Soft, Fiber-reinforced Bellow Actuators

Vi T. Vo[1], Leonardo Zamora Yañez[1], Casper Muter[1], Anna Maria Moran[1], Manvi Saxena[1], Grace Matthews[1], and Tommaso Ranzani[1,†]

Abstract—**Stacked balloon actuators, constructed from heat- and pressure-bonded, stacked layers of sheet films have demonstrated their utility in soft robotics for performing intricate tasks and adapting to space-constrained environments. However, these actuators face limitations such as reduced force output at low displacement heights due to buckling and small retractive forces at high displacement heights due to radial collapse under vacuum. To mitigate these issues, we introduce a method for integrating fiber reinforcements: a nylon mesh fabric that increases the tensile strength of the actuator's structural layers without constraining the maximum inflated height, and a heat-sealable nylon taffeta fabric that provides radial support to the actuator's multi-chamber design. We demonstrate the advantages of this approach in a quadruped soft robot, showcasing improved force output, actuation speed, and the advantageous use of actuator's collapsibility for shape morphing.**

Index Terms—**Soft Sensors and Actuators; Soft Robot Materials and Design; Soft Robot Applications**

I. INTRODUCTION

Fluidically actuated soft robots leverage their inherent flexibility and compliance to safely interact in unstructured environments [1]. Their ability to passively adapt and generate substantial actuation forces enables them to meet task-specific demands and handle environmental uncertainties effectively [2], [3]. This includes navigating through complex terrains [4] and interacting with delicate structures [5].

Inflatable soft actuators made from sheet materials have garnered increasing interest due to their monolithic fabrication, ease of manufacturability, and the lightweight nature afforded by the thinness of the sheet material [6]–[10]. Their manufacturing process typically involves a layer-by-layer fabrication approach or the selective bonding of stacked layers of thin polymer films and textiles [11]–[15]. This method enables a low-profile design in the unactuated state, maintaining a nearly zero resting volume, with the typical material thickness ranging from 100 to $350\,\mu\text{m}$ [11], [13], in contrast to elastomeric actuators which require various molds for distinct internal geometries, leading to large non-actuated volumes [3], [16]–[18].

Furthermore, inflatable actuators offer manufacturing flexibility by allowing shape and motion programming through geometric cut patterns or initially deflated shapes [19]–[21]. These actuators leverage controlled volumetric changes rather than relying on mechanical strain. Multi-DoF bellow-like actuators, in particular, extend their stroke in a preprogrammed manner using a stacked balloon architecture and enable independent expansion or contraction of their chambers for multi-directional movements [11]–[13]. Their collapsibility or the ability of the actuator to expand into the predesigned shape and retract back to its initial near-zero volume or flat configuration enables precise control and facilitates access to constrained spaces, including insertion through small apertures [22]–[24]. However, this bidirectional movement introduces specific challenges in force transmission: radial collapse may occur under tensile forces, leading to inward wall collapse, while under compressive loads, buckling or structural deformation can cause the actuator to bend instead of extending axially under pushing forces.

One approach to enhance force output in soft robots is to integrate soft and hard materials [12], [22]. However, reliable interfacial adhesion is critical, as differences in stiffness can cause mechanical failure from stress concentrations, and temperature incompatibilities can further complicate bonding.

Alternatively, the tensile strength of the structural layers composing the actuator can be increased. Fiber reinforcement in elastomeric actuators has been shown to improve the durability and force output while enabling mechanically programmable motion [25]–[28]. Textiles, in particular, offer a promising solution by providing durability, strength, and resilience, while retaining conformability [29], [30]. Since textiles cannot be thermally bonded directly, an additional thermoplastic polyurethane (TPU) layer can be used for adhesion. resulting in a heat-sealable textile widely used in soft wearables as the structural layers of pneumatic actuators [9], [13], [31]. However, increasing the thickness or stiffness of the textile layer reduces compliance and flexibility, limiting the actuator's ability to conform and adapt to various shapes and movements, and the resulting actuator typically requires higher operating pressures to achieve full inflation. Thus, achieving a balance between material robustness and the requisite flexibility is essential.

Herein, we present an approach to integrate fiber reinforcements into multi-DoF bellow actuators, or stacked balloon actuators (SBAs) by incorporating two additional materials: (i) a two-way stretch hexagonal mesh fabric and (ii) a heat-sealable nylon taffeta fabric. The mesh fabric enhances the tensile strength of the actuator's structural layers, allowing it to achieve higher force output while maintaining flexibility. The nylon taffeta fabric provides radial support for the multi-
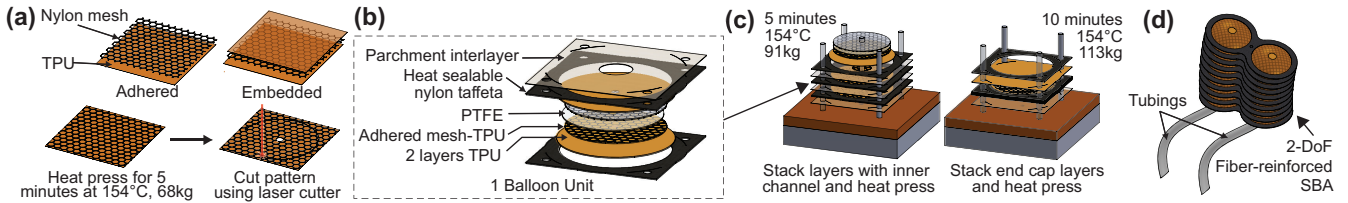
Fig. 1. **Overview of the fiber-reinforced SBAs fabrication process.** (a) Material preparation. (b) Stacked arrangements of the layers to create a single balloon unit. (c) Assembly of the fiber-reinforced SBAs by repeating the single balloon units separated with a parchment interlayer to define the bonding area. The center hole of each layer forms the flow path for fluid to inflate the actuator. The end cap piece is added in addition to the final ring of the nylon taffeta to seal and form the actuator. (d) Fully assembled fiber-reinforced SBA.

DoF bellow actuators to prevent overinflation and reduce the likelihood of excessive strain in the balloon structures. We demonstrate how integrating fiber-reinforced soft actuators enhances the design and functionality of a soft quadruped robot, showcasing locomotion capabilities through rapid actuation, weight-bearing support, and adaptable shape-morphing for navigation in constrained environments.

II. DESIGN AND MANUFACTURING

The fabrication of fiber-reinforced SBAs involves the use of a composite sheet material, comprising a nylon tulle with hexagonal mesh (SR-DTulleNT52-Blk, Vogue Fabrics) and $38\,\mu m$-thick layers of TPU (American Polyfilm). The composite consisting of nylon hexagonal mesh fabric and TPU is fabricated by heat pressing the layers in two arrangements: adhered where the mesh is bonded to a single layer of TPU or embedded where the mesh is sandwiched between layers of TPU (Fig. 1(a)). The resulting composite sheet can then be patterned with a laser cutter to define the actuator's geometry.

With the composite sheets, we constructed the fiber-reinforced two-DoF SBAs with an inner diameter of $21\,mm$ and 10 connected balloons. The actuators feature two interconnected chambers that can bend in perpendicular directions by inflating each chamber independently, facilitating planar bending motions.

A single balloon unit is fabricated with a layer of heat-sealable nylon taffeta, TPU-side facing two adjacent layers of TPU, and an adhered mesh-TPU composite with the mesh fabric oriented towards the polytetrafluoroethylene (PTFE) (Fig 1(b)). The pattern is then reversed to form the other half of the balloon. This results in a total of three TPU layers forming each half of the balloon. Bonding the mesh with three layers of TPU ensures an airtight composite. The $25\,\mu m$-thick PTFE (8569K15, McMaster) layer acts as the masking layer to define the internal volume of the balloon geometry upon inflation by preventing the adhesion between layers of TPU. Each balloon unit is separated by parchment paper, which can be trimmed and removed following the final press. The actuator is reinforced with an inextensible fabric (FHSO-BLACK, Seattle Fabrics, Inc.) to limit radial deformation while maintaining the SBA's flexibility. The layers are cut using a 60-Watt CO_2 laser cutter (VLS 6.60, Universal Laser Systems) at laser settings of 50% power, 100% speed, and 1000 ppi for most materials and 3% power, 10% speed, and 1000 ppi for parchment paper. The layers are then stacked manually and aligned using dowel pins (Fig. 1(c)). Multiple balloon units can be stacked to

tune the stroke length of the actuator. We then insert tubing with an outer diameter of $1\,mm$ and an inner diameter of $2\,mm$ (5233K111, McMaster) as fluidic lines and seal the connections using superglue (524540, Loctite), resulting in the fiber-reinforced SBAs illustrated in Fig. 1(d).

III. MODELING

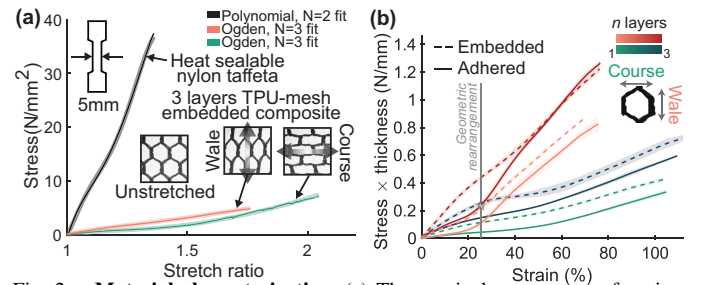### A. Uniaxial Strength Testing of Materials

Fig. 2. **Material characterization**. (a) The nominal stresses as a function of the ratio between the extended length and the initial length (i.e., the stretch ratio) for the heat-sealable nylon taffeta fabric and the three layers TPU-mesh embedded composite stretch in the wale and course direction. (b) Uniaxial testing data for the mesh-adhered and mesh-embedded samples stretched in the wale and course direction. Each curve represents the mean of three trials, with the shaded error bar indicating one standard deviation.

To understand the mechanical behavior of composite TPU materials, a tensile stress-strain test (ISO 37 standard) using the universal testing machine (5943, Instron) is conducted on the various layer arrangements and orientations of the mesh and TPU combinations relative to the strain direction. The samples are constructed and cut into dogbone patterns of $5\,mm$ in width and $28\,mm$ in gauge length, oriented along either fiber direction or the two directions of hexagonal cells in fillet knitted structures (Fig. 2(a)). The orientation of the hexagonal cells is determined by the alignment of their vertices along the wale (longitudinal) and course (transverse) directions (Fig. 2(a)). These samples are secured using pneumatic grippers (2712-052, Instron) with sandpaper to prevent slippage during testing and pulled lengthwise at a rate of 10 mm/min until failure occurred (i.e., the mesh tore); force and displacement are recorded during each trial. We characterized the material stiffness by plotting the sheet stress, defined as the product of engineering stress and initial thickness, against the engineering strain.

Experimental results indicated that samples incorporating embedded mesh exhibited greater tear strength compared to

those with adhered mesh, as illustrated in Fig. 2(b). We hypothesized that in the hexagonal mesh fabric, the interlooping between the hexagonal units undergoes geometric rearrangement, rather than stretching the material, during initial deformation. This rearrangement minimizes stress at low strains by adjusting the mesh spacing without significantly stretching the fibers. However, embedding the mesh constrains such unfolding due to the adherence of the TPU layers. Moreover, samples cut in the wale direction exhibited lower strength compared to those cut in the course direction, with the wale direction showing a maximum sheet stress of $\approx 1.26\,\mathrm{Nmm^{-1}}$ and the course direction $\approx 0.595\,\mathrm{Nmm^{-1}}$. This can be explained by the anisotropic properties of knitted mesh structures. The knitting architecture or intertwining and twisting patterns of the fibers create directional variations in mechanical performance, resulting in differing tensile strengths and deformation characteristics along the wale and course directions.
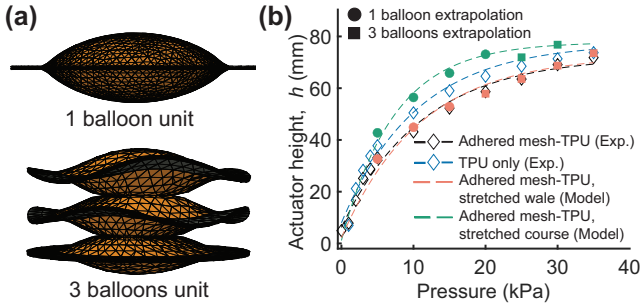

Fig. 3. **Stroke characterization**. (a) FEM results for the pressurization of single and 3-balloon unit fiber-reinforced SBAs. (b) Comparison of experimental and simulation results for the actuator height under pressurization.

B. Fitting to Models of Hyperelasticity in Abaqus

Hyperelastic models have been developed for the three materials used in the actuator fabrication. Using the experimental data from the uniaxial stretch test in Section III-A., we identified the hyperelastic material model that best predicted the material behavior in ABAQUS. To simplify our analysis, we assumed that the mesh-TPU composite, when stretched along a specific direction (i.e., either the wale or course direction), behaves homogeneously throughout. We then determined the corresponding coefficients for the selected model. The stretch-strain results for the TPU-mesh composite in the wale and course directions were fitted to the Ogden hyperelastic model ($N = 3$) with coefficients $\mu_1 = 158.32$, $\mu_2 = 2.47$, $\mu_3 = 69.89$, $\alpha_1 = 2.98$, $\alpha_2 = 92.94$, $\alpha_3 = 1.89$, and $\mu_1 = -19.33$, $\mu_2 = 1.00$, $\mu_3 = 8.71$, $\alpha_1 = 2.72$, $\alpha_2 = 13.20$, $\alpha_3 = 3.02$. In contrast, the heat-sealable nylon taffeta's stretch-strain results were fitted to a Polynomial ($N = 2$) or Mooney-Rivlin hyperelastic model with coefficients $C_{10} = 71.42$, $C_{20} = -1763.58$, $C_{01} = -54.54$, $C_{11} = 4552.77$, and $C_{02} = -2968.19$.

C. Modeling Stroke Length of Actuator

To evaluate the elongation of the fiber-reinforced actuator, we developed a finite-element model (FEM) to predict the

mechanical behavior. We simulated the expansion of a 1-DoF fiber-reinforced SBA using ABAQUS Standard element library (Fig. 3). For the analysis, we designed half of the balloon and formed a single balloon by applying surface-to-surface constraints where the TPU bonds with an inner pocket by creating a parabolic curve to the vertical cross-sectional boundary of the balloon of thickness $20\,\mu\mathrm{m}$ with a diameter of $21\,\mathrm{mm}$ to introduce internal surfaces for uniform static pressure load. Two regions are defined to assign material properties of the two custom materials: nylon taffeta and three layers TPU-mesh composite stretch in either the wale or course direction (Fig. 3(a)). A mesh is created using ten-node tetrahedral element type (C3D10) with hybrid formulation, quadratic geometric model, and a global element seed size of $1.6\,\mathrm{mm}$ and a total number of 12104 elements. Next, we applied edge constraints to interconnect the balloons and define the bonding region between each balloon unit. The actuator height is determined by summing the height of the top balloon, which domes due to the unconstrained top, the combined heights of the center balloons, each adjusted for the bonding areas, and the height of the bottom balloon, which is influenced by the anchored surface. The results of the FEM model are discussed in Section IV-A.
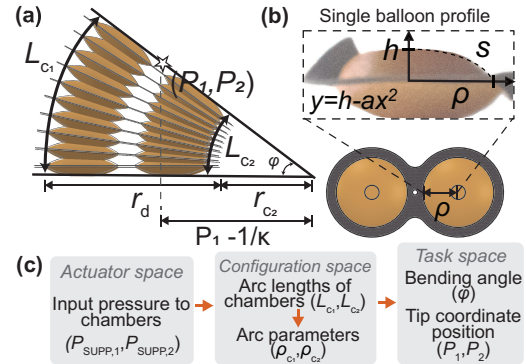
D. Modeling Bending Angles of Actuator

Fig. 4. **Actuator geometry and kinematic mapping of actuators**. Schematic representation of the 2-chamber fiber-reinforced SBA in bending configuration including (a) fitting an arc to the actuator for bending angle calculations and (b) a cross-sectional view of a single balloon, used to derive the inflated radius of the balloon. (c) Parameters involved in the motion of the SBA in 2D-space. The actuator's geometric configuration, including the arc length and how the individual balloons change shape, depends on the input pressures. The configuration space maps to the task space, defined by the orientation and position of the robot's tip, following geometric analysis.

Understanding the bending angle of the 2-DoF fiber-reinforced SBA is important for defining the actuator's range of motion. We developed a semi-empirical model that combines experimental data with geometric analysis to predict the bending angle. Experimental data were used to map input pressure to the corresponding inflation height, which was then used in a geometric model to determine the bending angle (Fig. 6(b)). The nonlinear deformation of the actuator under varying internal pressures was approximated by evaluating the arc lengths of the inflated balloons at different pressure levels, employing a fitted function that relates pressure to elongation, as shown in Fig. 3(b). The geometric model

assumes the inextensibility of the TPU, describing the SBA inflation only up to the point before the material begins to strain. In other words, during inflation, the balloon undergoes a geometric unfolding from a flat to an expanded state, with the material itself remaining unstretched.

The bending angle (ϕ, see Fig. 4(a)), can be derived geometrically and is determined by assuming that the two arc lengths have the same bending angle, setting the relationship $L_{c_1}(r_d + r_{c_2}) = L_{c_2} r_{c_2}$.

$$h = \frac{h_{deflate} + L_{c_i}}{2N} \tag{1}$$

$$r_{deflate} = \int_0^\rho 1 + (-2\alpha x)^2 \, dx \tag{2}$$

$$r_{c_2} = \frac{L_{c_2}(r_{nylon} + 2\rho_{c_1} + 2\rho_{c_2})}{|L_{c_1} - L_{c_2}|} \tag{3}$$

We defined the lengths of the outer chamber as the outer perimeter and the inner chamber as the inner perimeter of the actuator shape (Fig. 4(a)). Additionally, to account for the changing radius of the balloons as they inflate, we follow the mathematical formulations for an inflated mylar balloon by Paulsen et al [32]. We modeled the cross-sectional area of the balloon as a parabolic curve. Thus, the equation of the curve for the arc length is defined by $y = h - \alpha x^2$ where h is the height of one half of the balloon cut latitudely (see (Eq. 1)) and α is the coefficient that describes the width of the parabola (Fig. 4(b)). The cross-sectional boundary conditions constrains the arc length s to be equal to the deflated radius of the balloon, $r_{deflated}$ (= 10.5 mm). The inflated radius of the balloon ρ was then solved numerically using MATLAB from (Eq. 2), substituting $\alpha = \frac{h}{\rho^2}$ derived following $y(x = \rho) = 0 = h - \alpha \rho^2$ which defines the boundary condition of the parabolic curve and h from (Eq. 1) with $h_{deflate} = 4.95$ mm and $N = 10$ balloons. The distance between the arc lengths formed by the inner and outer chambers r_d is equivalent to the summation $2\rho_{c_1} + 2\rho_{c_2} + r_{nylon}$ (Fig. 4(a)). The estimated bending angle of the actuator is then calculated as $\frac{L_{c_2}}{r_{c_2}}$ where r_{c_2} is calculated following Eq.3 with $r_{nylon} = 5.5$ mm.

IV. ACTUATOR CHARACTERIZATIONS

A. Stroke Characterization

To validate the FEM model predicting actuator extension in Section III-B, we collected experimental data on stroke length as a function of input pressure. We fixed one end of the SBA to a plate on the Instron 5943 and measured displacement by zeroing the load cell at initial contact and then again after raising the actuator, repeating this process for incremental pressure increases of 5 kPa. Fig. 3(b) shows the stroke length of the actuator as a function of input pressure up to 35 kPa. The results show an agreement between the experimental expanded height of the fiber-reinforced SBA and the ABAQUS model for the composite stretched in the wale direction, with a mean error of 0.82 mm (Fig. 3(b)). This observation suggests that the actuator's expansion is preferentially oriented along the wale direction, likely due to the fiber reinforcement's

behavior during inflation. Specifically, the biaxial expansion of the actuator facilitates easier stretching of the fibers along the wale direction, resulting in deformation predominantly in that orientation. This behavior is supported by the stress-strain curve in Fig. 2(b), which indicates higher stress along the wale for the same strain compared to the course direction. The fiber-reinforced SBA achieves a maximum stroke length of ≈ 67 mm with a deflated height of 4.95 mm, whereas the non-reinforced reaches a stroke length of 71 mm at the same pressure with a deflated height of 2.70 cm. The fiber-reinforced actuator retains a substantial portion of its inflation height, demonstrating that the reinforcement approach does not significantly compromise the actuator's stroke length.

B. Pushing Force Characterization

We characterized the blocking force of the fiber-reinforced actuator using a setup that included a universal testing machine (5943, Instron) configured with a 50 N load cell, see Fig. 5(a). The internal pressure of the actuator is controlled by pressure regulators (ITV0010, SMC Corporation Tokyo) connected to a compressed air supply (Fig. 5(b)). We increased the pressure from 5.0 kPa to 35.0 kPa in 5.0 kPa increments. Fig. 5(c) reports the results from force versus pressure tests for the 2-DoF SBAs, both fiber-reinforced and TPU-only (fabricated with three layers of TPU), during extension at various elongation heights. Both the fiber-reinforced and TPU-only actuators initially generate comparable forces of 17.1 N in the flat configuration. The force produced by the SBAs is directly proportional to both the internal pressure and the effective cross-sectional area in contact with the load cell. At this elongation, both actuators exhibit identical effective areas, resulting in similar force outputs. However, at higher displacements, material-specific properties, such as stiffness, become increasingly significant. At 25% max elongation, the TPU-only SBAs experience significant buckling resulting in notable reduction in the force output. The TPU-only SBAs generate a maximum force of 9.9 N while the fiber-reinforced SBAs generates 14 N, indicating $\approx 41\%$ improvement in force output. The TPU-only SBAs show a higher standard deviation in maximum force, resulting indicating higher variability. Buckling occurs when the applied load exceeds the material's capacity to resist deformation resulting in bending of the actuator. This deformation reduces the effective contact area with the load cell and thus decreases the actuator's force output as shown in the inset of the TPU-only SBA in Fig. 5(c)-i. At 50% elongation and 75% elongation, the peak force measured is 6.4 N and 2.4 N for the fiber-reinforced actuators, respectively, compared to 2.1 N and 1.9 N for the TPU-only actuators. This represents a 204.8% increase in force output at 50% elongation and a 20.8% increase at 75% elongation for the fiber-reinforced SBAs compared to TPU-only.

C. Pulling Force Characterization

To evaluate the actuator's ability to resist buckling under applied negative pressure, we secure its ends to a flat plate attached to the load cell of a testing machine. The top and bottom acrylic fixtures are positioned at the elongation height
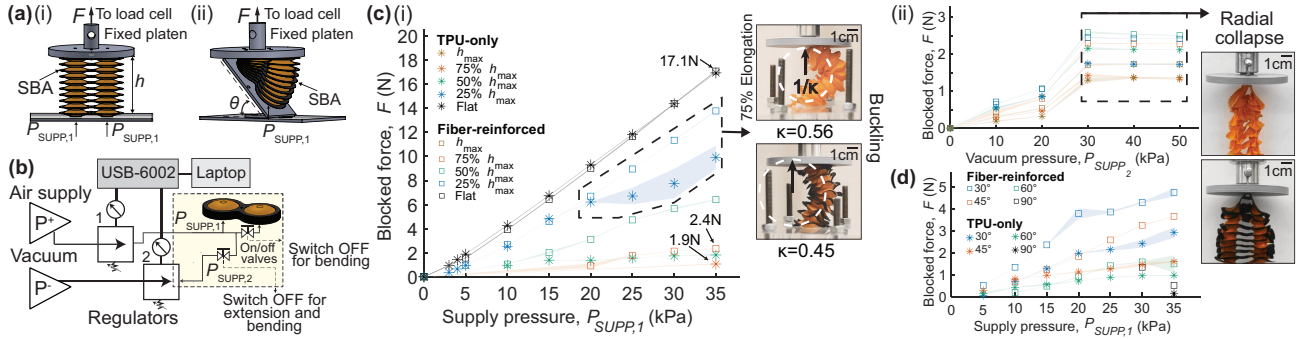
Fig. 5. **Force characterization**. (a) Schematic of the experimental setup for force characterizations in (i) extension, retraction, and (ii) bending. (b) Schematic of the electropneumatic circuit. (c) Blocked force results for a 10-balloon, 2-chamber fiber-reinforced and TPU-only SBA (i) inflated against a load cell (inset shows the buckling of the TPU-only SBA at 75% elongation) and (ii) depressurized at four different height increments to measure the force output at each pressure level (inset shows fiber-reinforced and TPU-only SBAs under a vacuum of $-50\,\mathrm{kPa}$ at the same displacement). (d) Force generated by a 10-balloon, 2-chamber fiber-reinforced and TPU-only SBA inflated against a load cell at four bending angles. The shaded bar represents the means and standard deviations from three trials at each pressure.

distance before applying a negative pressure ranging from $0\,\mathrm{kPa}$ to $-50\,\mathrm{kPa}$ in increments of $-10\,\mathrm{kPa}$. The pulling force is then measured as the actuator retracts from its initial fixed height. The fiber-reinforced actuators exhibit peak forces of $2.59\,\mathrm{N}$ at 50% elongation, $2.45\,\mathrm{N}$ at 25% elongation, $2.29\,\mathrm{N}$ at 75% elongation, and $1.71\,\mathrm{N}$ at 100% elongation under vacuum conditions. In comparison, the TPU-only actuators show peak forces of $2.15\,\mathrm{N}$ at 50% elongation, $1.74\,\mathrm{N}$ at 25% elongation, $1.42\,\mathrm{N}$ at 75% elongation, and $1.30\,\mathrm{N}$ at 100% elongation. This results in an average increase of $\approx 39.5\%$ in force output for the fiber-reinforced actuators compared to the TPU-only actuators. The observed reduction in force after the peak value at $30\,\mathrm{kPa}$ is attributed to the progressive inward compression with increasing negative pressure, as shown in the inset in Fig. 5(c)-ii. We also observe that for the fiber-reinforced actuators, the peak force between 25% and 75% elongation are within similar ranges, with values ranging from $2.58\,\mathrm{N}$ to $2.29\,\mathrm{N}$. However, the force decreases at 100% elongation, where it decreases to $1.71\,\mathrm{N}$, representing a reduction of $\approx 34\%$ from the peak value at 50% elongation. The consistent force output of the fiber-reinforced actuators between 25% and 75% elongation indicates effective resistance to radial collapse under vacuum conditions, suggesting that the actuator's internal structure maintains stability within this range. However, the significant reduction in force at 100% elongation highlights the actuator's limitations, where increased radial collapse at maximum stretch leads to decreased performance. In contrast, the TPU-only SBA exhibits a significant decrease in force output from 50% to 100% elongation, dropping by $\approx 39.5\%$. Interestingly, both actuators achieve their peak force at 50% elongation rather than the expected 25% or lowest displacement height. We hypothesize that at 50% elongation, the actuator presents a larger effective area for the vacuum to act upon while not being excessively strained.

D. Force Characterization in Bending

The bending configuration test was conducted similarly to the extension test, except the SBA was secured to a 3D-printed jig angled to the load cell of the Instron, with only one chamber inflated to achieve the bending (Fig. 5(b)). As shown

in Fig. 5(d), the fiber-reinforced SBA exerts a maximum force of $4.67\,\mathrm{N}$ at $30°$, $3.59\,\mathrm{N}$ at $45°$, $1.52\,\mathrm{N}$ at $60°$, and $0.45\,\mathrm{N}$ at $90°$, compared to the TPU-only actuator, which produces $2.85\,\mathrm{N}$ at $30°$, $1.53\,\mathrm{N}$ at $45°$, $0.91\,\mathrm{N}$ at $60°$, and $0.09\,\mathrm{N}$ at $90°$. This represents an average increase of $\approx 166.88\%$ in force output for the fiber-reinforced actuator.
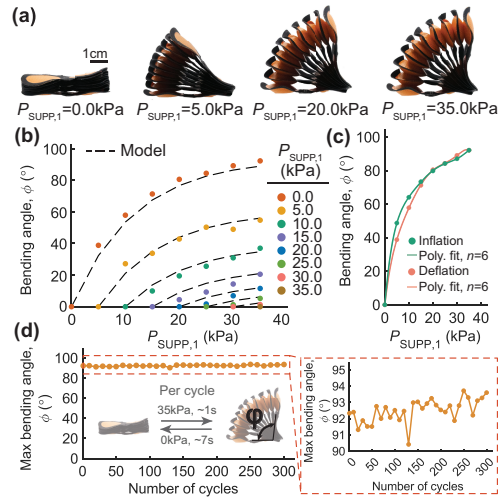
E. Bending Characterizations

Fig. 6. **Bending angle and curvature analysis of actuators** (a) Experimental results displaying the curvature of the SBA under various pressure levels. (b) Comparison between the experimentally measured bending angle of the actuator and the predictions obtained from the model. (c) Hysteresis behavior of the bending angle. (d) Experimental results of cyclic testing.

To quantify the deformation of the actuators under different input pressures, we employed a high-resolution camera to capture images of the actuator (Fig. 6(a)). Red dots, made from laser-cut pieces of electrical tape, are affixed along the edges of the center backbone on both the top and bottom surfaces to serve as visual markers. These images are then processed using MATLAB functions to identify the markers and their Cartesian coordinates. The two chambers are connected to separate air regulators, configured in parallel to a single constant pressure input. The pressures in each chamber are controlled using the pressure regulators connected to the National Instruments

USB-6002, similarly to the setup in Fig. 5(a). In the testing procedure, one chamber is set to a constant pressure while the other chamber's pressure is varied in $5\,\mathrm{kPa}$ intervals. For subsequent tests, the pressure of the first chamber is increased by $5\,\mathrm{kPa}$, and the varying pressure intervals are repeated for the second chamber.

We calculate the bending angle by approximating the arc length L_b as a sum of the distances between successive dots. The curvature κ is determined following $\kappa = 2P_1/(P_1^2 + P_2^2)$ where (P_1, P_2) is the coordinate position of the tip position following the center backbone (Fig. 4(a)). Subsequently, the bending angle is computed as the product of the arc length and curvature as κL_b. The theoretical bending angle is in good agreement with the experimentally observed bending angles with a mean error of $2.9°$. Some discrepancies may be attributed to the ballooning effect, which leads to radial expansion of the central backbone and introduces deformations not captured in the assumptions on the geometry of the SBAs. We characterized the hysteresis in the bending angle by plotting the angle as a function of input pressure during both the loading and unloading cycles (Fig. 6(c)). The resulting hysteresis loop exhibited both positive and negative areas, indicating a lag or overshoot in the bending response. The maximum hysteresis error was found to be $3.0°$, corresponding to 3.3% of the total bending angle range. This result suggests that the actuator's response is predominantly governed by geometric changes rather than material deformation. We also conducted cyclic testing by inflating ($P_{SUPP,1} = 35\,\mathrm{kPa}$) and deflating ($P_{SUPP,1} = 0\,\mathrm{kPa}$) the left chamber of the actuator over 300 cycles, during which we measured the change in bending angle after every 10 cycles. Tip position was tracked with an electromagnetic (EM) position tracking system (Aurora, Northern Digital Inc.). As shown in Fig. 6(d), the maximum bending angle consistently reached a mean of $92.5°$ with a standard deviation of 0.72. This small variation in the maximum bending angle across cycles indicates that the actuator's reliability and consistency under repeated actuation.

V. GROUND LOCOMOTION DEMONSTRATIONS

A. Design of Soft Quadruped Robot

We developed a soft quadruped robot with four 2-chamber, fiber-reinforced soft actuators (SBAs) attached to a platform 3D-printed from thermoplastic polyurethane (Flexfill TPU 98A, filamentum) as shown in Fig. 7(a). The robot's limbs are mounted perpendicularly to the plane of the platform such that when one chamber of a limb is pressurized, the actuator pushes on the ground to move the robot forward. We incorporated semi-circular cutouts of TPU into the feet of the robot to create asymmetric frictional forces as the actuators inflate, thereby facilitating forward movement and gait stability (Fig. 7(a)). We note that, while the 2-chamber actuator design supports basic locomotion, it limits the ability to perform the sweeping motion required for the creep gait, where one leg extends forward while the others provide stable support. Thus, the legs may remain bent as they drag, effectively providing necessary stability while the other legs push forward. Multi-chamber configurations may enable more dynamic movements

and omnidirectional control [33]. The robot without pneumatic tubings weighs $63.9\,\mathrm{g}$ and measures $12\,\mathrm{cm}$ in body length (BL), $8.5\,\mathrm{cm}$ in width, and $2\,\mathrm{cm}$ in height when deflated. As shown in Fig. 7(c), the robot can lift and sustain a $500\,\mathrm{g}$ load—≈ 7.8 times its body weight. Our fiber-reinforced SBAs achieve a high power density of $5.8\,\mathrm{kWkg^{-1}}$, comparable to millimeter-scale 3-chamber SBAs made with thermoplastic elastomer with reported value of $5.8\,\mathrm{kWkg^{-1}}$ [11] and higher than unidirectional actuators introduced in [34] with reported value of $2\,\mathrm{kWkg^{-1}}$. For comparison, soft elastomeric actuators typically exhibit power densities between $8\,\mathrm{Wkg^{-1}}$ and $0.5\,\mathrm{kWkg^{-1}}$ [35]. This high power density enables the robot to lift heavy loads and maintain mobility, making it ideal for tasks requiring both stability and force generation.

B. Walking Demonstration

We demonstrate the robot's ability to generate substantial forces and resist buckling, enabling it to stand upright and maintain stability throughout the gait cycle. The robot's diagonal gait pattern is illustrated in Fig. 7(d), where the movement sequence is controlled by the timing of the inflation and deflation cycles of each chamber. Inflating both SBA chambers at $35\,\mathrm{kPa}$ takes $1.07\,\mathrm{s}$, though manual inflation with a syringe achieves speeds of $39.6\,\mathrm{ms}$. Instead of controlling all eight chambers individually, we simplified the control scheme by pairing chambers diagonally, with the front chamber in each pair (Fig. 7(b)). Input lines for the chambers are linked together using push-to-connect fittings to be operated from a single input pressure. The other eight chambers are inflated by infusing $20\,\mathrm{mL}$ of air at the initial start of the gait Fig.7(d)-ii. Timed actuation of these pairs in sequence propels the robot forward, with the second pair inflating as the first deflates (Fig. 7(d)-iii). This coordinated movement achieves a forward motion at a speed of $5.8\,\mathrm{BL\,min^{-1}}$. Notably, this speed exceeds that of robots using elastomeric actuators, which typically achieve speeds ranging from $0.13\,\mathrm{BL\,min^{-1}}$ to $0.9\,\mathrm{BL\,min^{-1}}$ [4], [36], [37]. Pneumatic actuators often face challenges with slow response times, driven by the material's response characteristics, the volume that must be inflated, and weight of the actuators [16]. This limitation is particularly significant for locomotive soft robots, which demand rapid, dynamic actuation to navigate effectively. The response delay arises from the time required to fill the actuator's internal cavities and the subsequent material deformation needed to generate motion.

C. Navigation In Constrained Environment

Navigating confined spaces requires actuators that contract upon actuation to avoid hindering movement with increased volume. The robot demonstrates its ability to navigate constrained environments by bracing against surfaces to create a localized fixed constraint. This capability is illustrated by maneuvering the robot through two parallel plates space $5\,\mathrm{cm}$ apart. Initially, the robot's height prevents it from passing through the gap, causing it to be obstructed (Fig. 7(e)-i). To overcome this, the robot lowers its height by deflating its actuators, effectively morphing its body to fit through the gap.
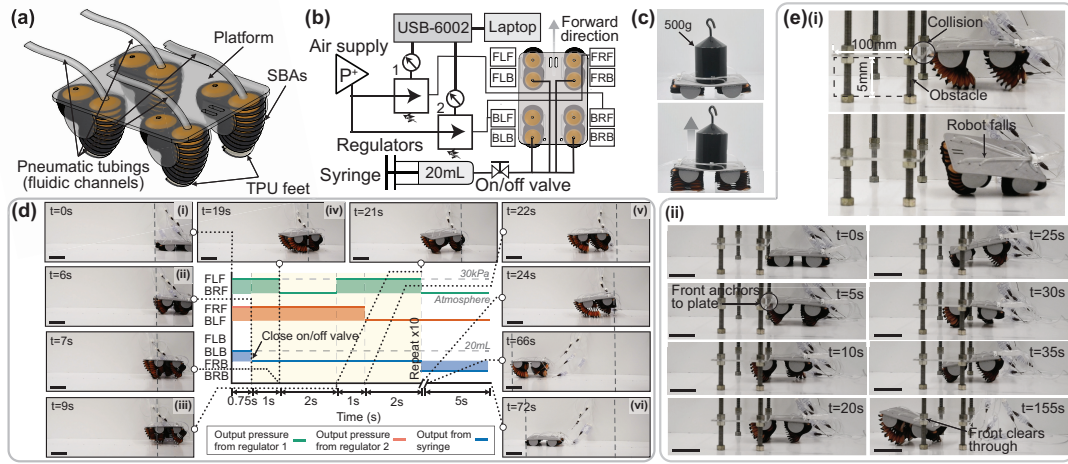
Fig. 7. **Soft robot leveraging the fiber-reinforced SBAs for locomotion** (a) CAD rendering of the tethered soft quadruped robot. (b) Schematic of the electropneumatic circuit to control the gait sequence. (c) The robot lifting $500\,\mathrm{g}$ weight. (d) Sequential images from Supplementary Video illustrating the gait cycle of the robot: (i) The robot starts in its deflated state (all actuators collapsed). (ii) All legs begin to lift, initiating the gait cycle. (iii) One pair of legs deflates while the other pair inflates to stabilize the robot. As the actuators inflate, the TPU feet make contact with the ground. The asymmetric friction, resulting from the contact angle during inflation, causes the actuators to bend forward, providing anchorage and propelling the robot forward. The deflation of the opposite pair reduces ground contact, facilitating forward movement. (iv) The gait cycle repeats, allowing the robot to continue moving forward. Here, after advancing, both pairs of actuators inflate to stabilize the robot. (vi) The robot traverses $\approx 70\,\mathrm{cm}$ before deflating back to its collapsed state. (d) The robot lifting a payload of 500g. (e) Sequential images showing the robot navigating through a constrained environment. (i) The robot encounters the obstacle, causing it to fall due to the height of its walking gait. (ii) The robot adjusts its gait to crawl underneath the obstacle, showcasing the effective morphing capabilities enabled by its collapsible actuators. The scale bars in the images represent $10\,\mathrm{cm}$.

To achieve this, we modified the gait used in the previous demonstration, described in Section III-B, by pairing the front and hind legs instead of the diagonal pairs. We also adjusted the actuation timing: the front legs inflate for $1\,\mathrm{s}$ seconds while the back legs deflate for $5\,\mathrm{s}$. Fig. 7(e)-ii illustrates the robot executing a crawling gait as it navigates through the constrained space. Although the robot's speed is relatively slow due to deflation time, our focus here is on demonstrating the shape-morphing capability of the robot enabled by the collapsibility of the actuators. An active vacuum could enhance speed but would introduce additional complexity and power demands. We opted to exhaust to the atmosphere to maintain system simplicity.

VI. CONCLUSIONS

We present a method for incorporating fiber reinforcements into soft bellow actuators using a layer-by-layer fabrication process. By integrating a hexagonal mesh to enhance tensile strength and nylon taffeta for radial support, we achieved reduced buckling at low displacement heights and mitigated radial collapse during retraction. This reinforcement not only improves the durability and mechanical properties of the actuators but also preserves their inherent advantages. Our use of thermoplastic materials with hyperelastic properties enables significantly greater expansion and longer stroke lengths while maintaining the ability to collapse into a compact, low-profile configuration when deflated (Fig. 6). From blocked force tests, the fiber-reinforced actuators demonstrate an average increase of 88.2% in pushing force and 39.5% in pulling force compared to TPU-only SBAs, with only a 5.6% reduction in stroke length and a maximum displacement of $66.8\,\mathrm{mm}$. To the authors' knowledge, there have been no prior efforts to incorporate fibers or mesh textiles into inflatable structures.

We developed a model of the TPU-mesh composite which predicts the actuator expansion in response to an input pressure with a mean error of $\approx 0.82\,\mathrm{mm}$, and a model to analyze the bending behavior of the actuators with a mean error of $2.9°$. We highlight three key advantages of fiber-reinforced SBAs used as limbs in a soft quadruped robot. First, the 2-DoF SBA inflates fully at approximately $35\,\mathrm{kPa}$ in just $1.07\,\mathrm{s}$, enabling the robot to maintain an effective gait. This rapid actuation is achieved through geometric unfolding, which prioritizes structural expansion over material strain. Additionally, the actuator's lightweight design ($6.2\,\mathrm{g}$) minimizes the risk of buckling under gravity.

Second, their ability to withstand high compressive loads makes them suitable for weight-bearing tasks and prevents deformation under operational stresses. The fiber reinforcement improves the robot's resistance to buckling, addressing a common limitation in soft robotics where actuators often struggle to support substantial payloads due to their restricted force generation [37].

Third, the collapsible nature of the actuators provides the robot with shape-morphing capabilities, allowing it to navigate constrained environments effectively. The robot can adapt its profile and utilize the compliance of the actuators to maneuver through a confined space. Moreover, the design of the fiber-reinforced SBAs facilitates a compact and lightweight operation, setting them apart from traditional motor-based systems. Operating at low pressures without the need for high currents or voltages enhances efficiency and safety. While other actuation mechanisms, such as shape memory alloys (SMAs) and electrostatic polymers, can achieve shape morphing through alternative means, our approach leverages fluidic actuation for fast, reversible motion profiles that excel in dynamic and adaptive environments [38]. However, this strategy requires

an external pressure supply and tubing to maintain a supply of compressed air for actuation. An alternative approach to design the hardware of the system should be considered for onboard fluidic control [39].

We emphasize that our focus in this work is not on optimizing locomotion speed or gait control. Future work will build upon this robotic platform, involving analysis of the inflation duration, relating to the time constant for each actuator chamber to reach and stabilize at the desired pressure, and actuator deflection upon ground contact. Understanding these dynamics and kinematics is essential for refining gait performance, which will enhance the robot's speed, payload capacity, and adaptability to diverse environments.

REFERENCES

[1] C. Laschi, B. Mazzolai, and M. Cianchetti, "Soft robotics: Technologies and systems pushing the boundaries of robot abilities," *Science robotics*, vol. 1, no. 1, p. eaah3690, 2016.

[2] P. Polygerinos, N. Correll, S. A. Morin, B. Mosadegh, C. D. Onal, K. Petersen, M. Cianchetti, M. T. Tolley, and R. F. Shepherd, "Soft robotics: Review of fluid-driven intrinsically soft devices; manufacturing, sensing, control, and applications in human-robot interaction," *Advanced engineering materials*, vol. 19, no. 12, p. 1700016, 2017.

[3] B. Gorissen, D. Reynaerts, S. Konishi, K. Yoshida, J.-W. Kim, and M. De Volder, "Elastic inflatable actuators for soft robotic applications," *Advanced Materials*, vol. 29, no. 43, p. 1604977, 2017.

[4] M. T. Tolley, R. F. Shepherd, B. Mosadegh, K. C. Galloway, M. Wehner, M. Karpelson, R. J. Wood, and G. M. Whitesides, "A resilient, untethered soft robot," *Soft robotics*, vol. 1, no. 3, pp. 213–223, 2014.

[5] K. C. Galloway, K. P. Becker, B. Phillips, J. Kirby, S. Licht, D. Tchernov, R. J. Wood, and D. F. Gruber, "Soft robotic grippers for biological sampling on deep reefs," *Soft robotics*, vol. 3, no. 1, pp. 23–33, 2016.

[6] A. Stilli, H. A. Wurdemann, and K. Althoefer, "Shrinkable, stiffness-controllable soft manipulator based on a bio-inspired antagonistic actuation principle," in *2014 IEEE/RSJ International Conference on Intelligent Robots and Systems*. IEEE, 2014, pp. 2476–2481.

[7] R. L. Baines, S. K. Patiballa, and R. Kramer-Bottiglio, "Rapidly reconfigurable inextensible inflatables," in *2021 IEEE 4th International Conference on Soft Robotics (RoboSoft)*. IEEE, 2021, pp. 29–34.

[8] R. Niiyama, X. Sun, C. Sung, B. An, D. Rus, and S. Kim, "Pouch motors: Printable soft actuators integrated with computational design," *Soft Robotics*, vol. 2, no. 2, pp. 59–70, 2015.

[9] F. Connolly, D. A. Wagner, C. J. Walsh, and K. Bertoldi, "Sew-free anisotropic textile composites for rapid design and manufacturing of soft wearable robots," *Extreme Mechanics Letters*, vol. 27, pp. 52–58, 2019.

[10] E. W. Hawkes, L. H. Blumenschein, J. D. Greer, and A. M. Okamura, "A soft robot that navigates its environment through growth," *Science Robotics*, vol. 2, no. 8, p. eaan3028, 2017.

[11] J. Rogatinsky, K. Gomatam, Z. H. Lim, M. Lee, L. Kinnicutt, C. Duriez, P. Thomson, K. McDonald, and T. Ranzani, "A collapsible soft actuator facilitates performance in constrained environments," *Advanced Intelligent Systems*, vol. 4, no. 10, p. 2200085, 2022.

[12] H. C. Lee, N. Elder, M. Leal, S. Stantial, E. Vergara Martinez, S. Jos, H. Cho, and S. Russo, "A fabrication strategy for millimeter-scale, self-sensing soft-rigid hybrid robots," *Nature Communications*, vol. 15, no. 1, p. 8456, 2024.

[13] H. D. Yang and A. T. Asbeck, "A layered manufacturing approach for soft and soft-rigid hybrid robots," *Soft Robotics*, vol. 7, no. 2, pp. 218–232, 2020.

[14] L. Cappello, K. C. Galloway, S. Sanan, D. A. Wagner, R. Granberry, S. Engelhardt, F. L. Haufe, J. D. Peisner, and C. J. Walsh, "Exploiting textile mechanical anisotropy for fabric-based pneumatic actuators," *Soft robotics*, vol. 5, no. 5, pp. 662–674, 2018.

[15] P. H. Nguyen and W. Zhang, "Design and computational modeling of fabric soft pneumatic actuators for wearable assistive devices," *Scientific reports*, vol. 10, no. 1, p. 9638, 2020.

[16] B. Mosadegh, P. Polygerinos, C. Keplinger, S. Wennstedt, R. F. Shepherd, U. Gupta, J. Shim, K. Bertoldi, C. J. Walsh, and G. M. Whitesides, "Pneumatic networks for soft robotics that actuate rapidly," *Advanced functional materials*, vol. 24, no. 15, pp. 2163–2170, 2014.

[17] P. Polygerinos, Z. Wang, K. C. Galloway, R. J. Wood, and C. J. Walsh, "Soft robotic glove for combined assistance and at-home rehabilitation," *Robotics and Autonomous Systems*, vol. 73, pp. 135–143, 2015.

[18] A. D. Marchese, R. K. Katzschmann, and D. Rus, "A recipe for soft fluidic elastomer robots," *Soft robotics*, vol. 2, no. 1, pp. 7–25, 2015.

[19] J. D. Greer, T. K. Morimoto, A. M. Okamura, and E. W. Hawkes, "Series pneumatic artificial muscles (spams) and application to a soft continuum robot," in *2017 IEEE International Conference on Robotics and Automation (ICRA)*. IEEE, 2017, pp. 5503–5510.

[20] H. Lee, N. Oh, and H. Rodrigue, "Expanding pouch motor patterns for programmable soft bending actuation: Enabling soft robotic system adaptations," *IEEE Robotics & Automation Magazine*, vol. 27, no. 4, pp. 65–74, 2020.

[21] J. Kwon, S. J. Yoon, and Y.-L. Park, "Flat inflatable artificial muscles with large stroke and adjustable force–length relations," *IEEE Transactions on Robotics*, vol. 36, no. 3, pp. 743–756, 2020.

[22] S. Becker, T. Ranzani, S. Russo, and R. J. Wood, "Pop-up tissue retraction mechanism for endoscopic surgery," in *2017 IEEE/RSJ International Conference on Intelligent Robots and Systems (IROS)*. IEEE, 2017, pp. 920–927.

[23] D. Van Lewen, T. Janke, H. Lee, R. Austin, E. Billatos, and S. Russo, "A millimeter-scale soft robot for tissue biopsy procedures," *Advanced Intelligent Systems*, vol. 5, no. 5, p. 2200326, 2023.

[24] J. Rogatinsky, D. Recco, J. Feichtmeier, Y. Kang, N. Kneier, P. Hammer, E. O'Leary, D. Mah, D. Hoganson, N. V. Vasilyev *et al.*, "A multifunctional soft robot for cardiac interventions," *Science Advances*, vol. 9, no. 43, p. eadi5559, 2023.

[25] S. Y. Kim, R. Baines, J. Booth, N. Vasios, K. Bertoldi, and R. Kramer-Bottiglio, "Reconfigurable soft body trajectories using unidirectionally stretchable composite laminae," *Nature communications*, vol. 10, no. 1, p. 3464, 2019.

[26] F. Connolly, P. Polygerinos, C. J. Walsh, and K. Bertoldi, "Mechanical programming of soft actuators by varying fiber angle," *Soft Robotics*, vol. 2, no. 1, pp. 26–32, 2015.

[27] Y. Shengda, T. Wang, and S. Zhu, "Research on energy consumption of fiber-reinforced fluidic soft actuators," *Smart Materials and Structures*, vol. 30, no. 2, p. 025036, 2021.

[28] V. Sanchez, K. Mahadevan, G. Ohlson, M. A. Graule, M. C. Yuen, C. B. Teeple, J. C. Weaver, J. McCann, K. Bertoldi, and R. J. Wood, "3d knitting for pneumatic soft robotics," *Advanced Functional Materials*, vol. 33, no. 26, p. 2212541, 2023.

[29] J. Xiong, J. Chen, and P. S. Lee, "Functional fibers and fabrics for soft robotics, wearables, and human–robot interface," *Advanced Materials*, vol. 33, no. 19, p. 2002640, 2021.

[30] V. Sanchez, C. J. Walsh, and R. J. Wood, "Textile technology for soft robotic and autonomous garments," *Advanced functional materials*, vol. 31, no. 6, p. 2008278, 2021.

[31] R. A. Shveda, A. Rajappan, T. F. Yap, Z. Liu, M. D. Bell, B. Jumet, V. Sanchez, and D. J. Preston, "A wearable textile-based pneumatic energy harvesting system for assistive robotics," *Science advances*, vol. 8, no. 34, p. eabo2418, 2022.

[32] W. H. Paulsen, "What is the shape of a mylar balloon?" *The American mathematical monthly*, vol. 101, no. 10, pp. 953–958, 1994.

[33] D. Drotman, S. Jadhav, D. Sharp, C. Chan, and M. T. Tolley, "Electronics-free pneumatic circuits for controlling soft-legged robots," *Science Robotics*, vol. 6, no. 51, p. eaay2627, 2021.

[34] S. Li, D. M. Vogt, D. Rus, and R. J. Wood, "Fluid-driven origami-inspired artificial muscles," *Proceedings of the National academy of Sciences*, vol. 114, no. 50, pp. 13 132–13 137, 2017.

[35] S. Russo, T. Ranzani, C. J. Walsh, and R. J. Wood, "An additive millimeter-scale fabrication method for soft biocompatible actuators and sensors," *Advanced Materials Technologies*, vol. 2, no. 10, p. 1700135, 2017.

[36] P. Rothemund, A. Ainla, L. Belding, D. J. Preston, S. Kurihara, Z. Suo, and G. M. Whitesides, "A soft, bistable valve for autonomous control of soft actuators," *Science Robotics*, vol. 3, no. 16, p. eaar7986, 2018.

[37] A. Yin, H.-C. Lin, J. Thelen, B. Mahner, and T. Ranzani, "Combining locomotion and grasping functionalities in soft robots," *Advanced Intelligent Systems*, vol. 1, no. 8, p. 1900089, 2019.

[38] W. Wang, N.-G. Kim, H. Rodrigue, and S.-H. Ahn, "Modular assembly of soft deployable structures and robots," *Materials horizons*, vol. 4, no. 3, pp. 367–376, 2017.

[39] A. M. Moran, V. T. Vo, K. J. McDonald, P. Sultania, E. Langenbrunner, J. H. V. Chong, A. Naik, L. Kinnicutt, J. Li, and T. Ranzani, "An electropermanent magnet valve for the onboard control of multi-degree of freedom pneumatic soft robots," *Communications Engineering*, vol. 3, no. 1, p. 117, 2024.